Insulator-metal transition in $Ru(Br_{1-x}I_x)_3$ with honeycomb structure

Fuki Sato,[1,*] Hideyuki Fujihara,[1] Hirotada Gotou,[2] Takuya Aoyama,[1] Yoshinori Imai,[1] and Kenya Ohgushi[1]
[1]*Department of Physics, Graduate School of Science, Tohoku University, 6-3 Aramaki-Aoba, Aoba-ku, Sendai, Miyagi 980-8578, Japan*
[2]*Institute for Solid State Physics, University of Tokyo, 5-1-5 Kashiwanoha, Kashiwa, Chiba 277-8581, Japan*

(Received 31 October 2023; revised 17 December 2023; accepted 5 January 2024; published 24 January 2024)

We investigate electronic properties of solid solution $Ru(Br_{1-x}I_x)_3$ with honeycomb structure which bridges the spin-orbit-entangled Mott insulator $RuBr_3$ and strongly electron-correlated semimetal RuI_3. We find a first-order insulator-metal transition at $x \sim 0.85$ triggered by increased d-p hybridization and formation of interlayer I–I bonds. We also observe switching of the magnetic structure at $x = 0.30$. In the metallic phase, we find critical mass enhancement leading to the carrier localization. This study furthers understanding of the Mott transition in a strongly spin-orbit-entangled system.

DOI: 10.1103/PhysRevB.109.035154

Exotic quantum phenomena such as high-temperature superconductivity and giant magnetoresistance appear near the Mott transition in 3d transition-metal compounds [1]. Recently, research has been extended to 4d and 5d transition-metal compounds, where strong spin-orbit coupling is expected to trigger the emergence of new electronic properties [2]. For example, compounds of the form $Ca_{1-x}Na_xIrO_3$ with postperovskite structure exhibit a strange metallic phase related to antiferromagnetic fluctuations near the Mott transition [3]. Another example is the family $R_2Ir_2O_7$ (R = rare − earth element), which has pyrochlore structure showing Weyl-semimetal behavior [4].

We here focus on the 4d transition-metal compound α-$RuCl_3$, which has been attracting considerable attention as a Kitaev spin-liquid candidate material [5,6]. The material has a honeycomb network of Ru^{3+} ions formed by edge-shared $RuCl_6$ octahedra in the ab plane [7]. The strong spin-orbit coupling and on-site Coulomb repulsion lead the system into a spin-orbit-coupled Mott-insulator phase with half-filled $j_{\rm eff} = 1/2$ bands [8]. In contrast to expectations of a Kitaev spin liquid, the non-Kitaev interactions lead to a zigzag antiferromagnetic order below $T_{\rm N} = 7$ K [9]. This zigzag antiferromagnetic order is suppressed under a magnetic field parallel to the ab plane, where possible realization of a chiral spin liquid is under intense debate [10–12].

Very recently, the isostructural materials $RuBr_3$ and RuI_3 (the $R\bar{3}$ space group) were successfully synthesized under high pressure [13–15]. Like α-$RuCl_3$, $RuBr_3$ is a spin-orbit-coupled Mott insulator with half-filled $j_{\rm eff} = 1/2$ bands and exhibits a zigzag magnetic order below $T_{\rm N} = 34$ K [13,16]. The higher $T_{\rm N}$ value in comparison with α-$RuCl_3$ is interpreted as being due to the stronger d-p hybridization resulting in a larger long-range exchange interaction, which causes the stabilized antiferromagnetic order [13]. In contrast to $RuBr_3$, RuI_3 shows semimetallic electrical conduction and Pauli paramagnetism. *Ab initio* calculations reveal that the on-site Coulomb repulsion is reduced in RuI_3 by the strong d-p hybridization, which is a key to the metallic behavior [14,17]. Hence one can expect solid solution $Ru(Br_{1-x}I_x)_3$ to be a good platform for investigating a bandwidth-controlled Mott transition in a 4d electron system.

In this paper, we investigate the insulator-metal transition in $Ru(Br_{1-x}I_x)_3$ via electrical resistivity, magnetic susceptibility, and specific heat. The results are summarized in Fig. 1. A first-order insulator-metal transition occurs at $x \sim 0.85$, where formation of an interlayer I–I bond plays an important role. In the insulating phase, $T_{\rm N}$ nonmonotonically changes with the halogen composition x, which indicates a magnetic structure switch at $x = 0.30$. In the metallic phase, the Sommerfeld coefficient γ is modestly enhanced near the Mott transition, which means that the carrier localization is due to the mass enhancement.

Polycrystalline samples of $Ru(Br_{1-x}I_x)_3$ were synthesized using a wedge-type cubic-anvil high-pressure apparatus. The starting materials were a stoichiometric mixture of $RuBr_3$ with a chain structure (2N; Mitsuwa Chemicals) and RuI_3 with a chain structure (∼95%; Mitsuwa Chemicals). The mixture was placed in a boron nitride (BN) capsule and loaded into a pyrophyllite cube. The pyrophyllite cube was pressurized at 2.2 GPa and then heated at 700 °C for 30 min. The samples were characterized via powder x-ray diffraction (PXRD) using Cu $K\alpha$ radiation at room temperature. The electrical resistivity ρ was measured using a four-terminal method using a physical property measurement system (PPMS; Quantum Design) at 2–300 K under a magnetic field of 0–9 T. The magnetic susceptibility χ was measured using a superconducting quantum interference device magnetometer. The specific heat C was measured with a thermal relaxation method using the PPMS.

All the peaks of the PXRD patterns are indexed as a honeycomb structure with the space group $R\bar{3}$ reported in Refs. [13–15], indicating successful synthesis of solid solution $Ru(Br_{1-x}I_x)_3$. The lattice parameters are estimated from the PXRD patterns, and we plot the intralayer Ru–Ru distance $d_{\rm Ru}$ and interlayer Ru–Ru distance $d_{\rm Layer}$ against the

*fuki.sato.r4@dc.tohoku.ac.jp

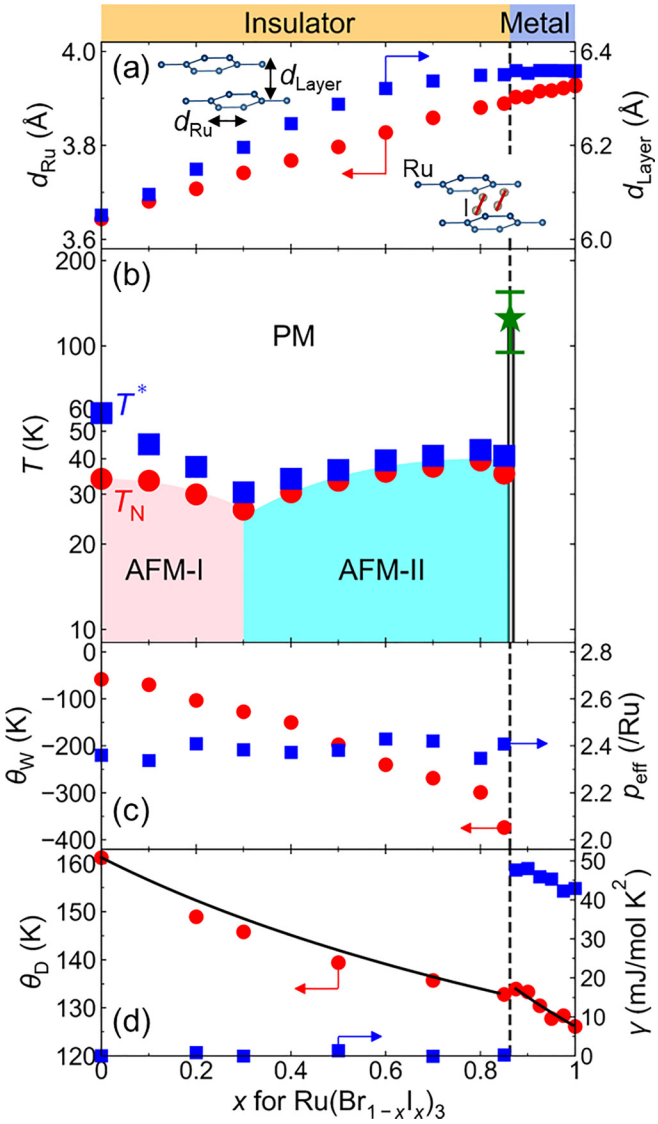

FIG. 1. Electronic phase diagram of $Ru(Br_{1-x}I_x)_3$. The black dashed line in this figure shows the composition $x = 0.85$, where the insulator-metal transition occurs. (a) Intralayer Ru distance d_{Ru} and interlayer Ru distance d_{Layer}. The insets are diagrams of the formation of an interlayer I–I bond [18]. (b) Antiferromagnetic transition temperature T_N and characteristic temperature T^* below which antiferromagnetic correlation develops. PM and AFM, paramagnetic and antiferromagnetic phases, respectively. The star at $x \sim 0.85$ represents the end point of the first-order insulator-metal transition. (c) Weiss temperature θ_W and effective magnetic moment p_{eff} estimated by fitting the magnetic susceptibility at 150–300 K. (d) Debye temperature θ_D and Sommerfeld coefficient γ estimated by fitting the specific heat at 2–5 K. The black solid curve indicates the results of applying the Neumann-Kopp law.

composition x in Fig. 1(a). One can see that the lattice expands with increasing x at $0 \leqslant x \leqslant 0.85$, whereas the interlayer distance shows saturation at $0.85 \leqslant x \leqslant 1$. This suggests a structural instability at $x \sim 0.85$; for example, an interlayer I–I bond forms at $0.85 \leqslant x \leqslant 1$. We were not able to observe new peaks associated with a structural transition in our PXRD patterns. However, such low-intensity superlattice peaks are possibly detected by single-crystal structure analysis.

Figure 2(a) shows the temperature T dependence of the electrical resistivity ρ for $Ru(Br_{1-x}I_x)_3$. As x increases, ρ gradually decreases, and the insulator-metal transition occurs at $x \sim 0.85$. Figure 2(b) shows the composition dependence of ρ at selected temperatures. At 2–100 K, there is a ρ jump of two orders of magnitude across the insulator-metal transition, indicating the first-order nature of the insulator-metal transition. However, at $T > 100$ K, ρ changes continuously. These behaviors indicate that the end point of the first-order transition is at $T = 100$–150 K. This end point is shown as a green star in Fig. 1(b).

We discuss the detailed T dependence of ρ. The ρ data at $x = 0$ follow simple thermal-activation behavior of the form $\rho = \rho_0 \exp(E_g/k_B T)$ with $E_g \sim 0.21$ eV [13]. However, insulating samples with $x \neq 0$ show a complicated T dependence. One can see that the diverging tendency of ρ at $x = 0.50, 0.70$, and 0.85 is weakened below $T = 250$, 160, and 40 K, respectively [each is marked as a solid triangle in Fig. 2(a)]. This behavior is well understood if one supposes that thermally activated carriers are accommodated into multiple bands with different electrical conductivities, in other words, with different effective masses or scattering times. This hypothesis is supported by first-principles calculations, which indicate that the entanglement of $j_{eff} = 1/2$ and $3/2$ bands with distinct band characteristics is enhanced going from $RuBr_3$ to RuI_3 [19].

This multicarrier feature of electrical conduction is also discernible in the metallic phase. As seen from Fig. 2(c), ρ at $x = 1$ has two bending points at $T \sim 100$ and 250 K. This indicates that ρ does not follow a simple Bloch-Grüneisen formula. Instead, this behavior can be well understood as multiple bands with different electrical conductivities participating in electrical conduction [20]. At $x = 0.875$–0.975, there is an upturn at $T < 40$ K. This upturn can be well fitted with a function proportional to $1/\sqrt{T}$ [inset of Fig. 2(c)], indicating three-dimensional weak localization due to a halogen-site randomness.

Figure 3 shows the T dependence of the magnetic susceptibility χ for $Ru(Br_{1-x}I_x)_3$. At $x = 0$–0.85, χ shows Curie-Weiss behavior. Meanwhile, at $x = 0.875$–1, χ shows Pauli paramagnetic behavior. This observation is consistent with the electrical resistivity data. As will be described below, we observed an antiferromagnetic transition in the insulating phase. On the other hand, there is no signature of an antiferromagnetic transition in the metallic phase [21], and the insulator-metal transition accompanies the collapse of the antiferromagnetic order. This is most likely related to the semimetallic feature of this system; in other words, a very small Fermi surface cannot form magnetic moments that are long enough for long-range antiferromagnetic order.

We now discuss χ in the insulating phase. The data for the high-T paramagnetic phase ($T = 150$–300 K) are well fitted with the Curie-Weiss law $\chi = N_A \mu_B^2 p_{eff}^2 / 3k_B(T - \theta_W)$, where p_{eff} is the effective magnetic moment, θ_W is the Weiss temperature, N_A is the Avogadro constant, μ_B is the Bohr magneton, and k_B is the Boltzmann constant. The thus-obtained parameters are plotted against x in Fig. 1(c). The effective magnetic moment p_{eff} is almost x independent, and

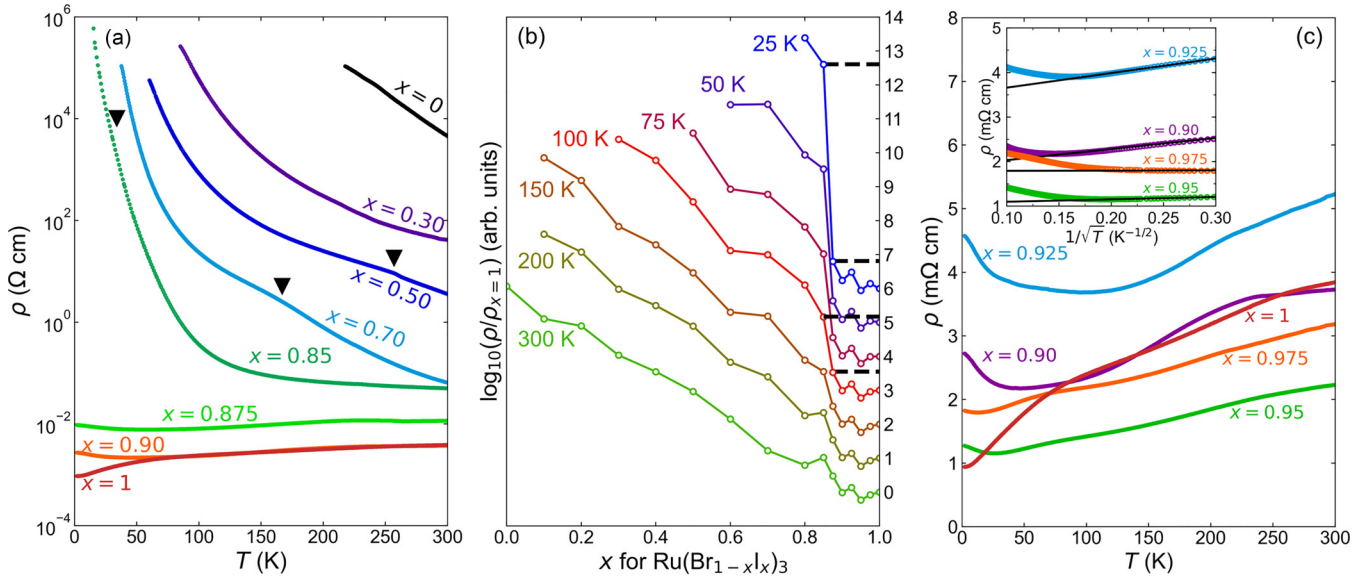

FIG. 2. (a) Temperature T dependence of electrical resistivity ρ for $Ru(Br_{1-x}I_x)_3$. Each solid triangle shows the value of T where the divergent tendency of ρ is suppressed. (b) Isothermal ρ data plotted against x for $Ru(Br_{1-x}I_x)_3$. (c) T dependence of ρ in the metallic phase for $Ru(Br_{1-x}I_x)_3$. The inset shows results of fitting with the $1/\sqrt{T}$ law in the localization regime.

the observed $p_{\rm eff}$ value of ∼2.4 is slightly larger than the theoretically expected value of 1.73 for a $j_{\rm eff} = 1/2$ electron. This is likely related to the strong spin-orbit coupling [22],

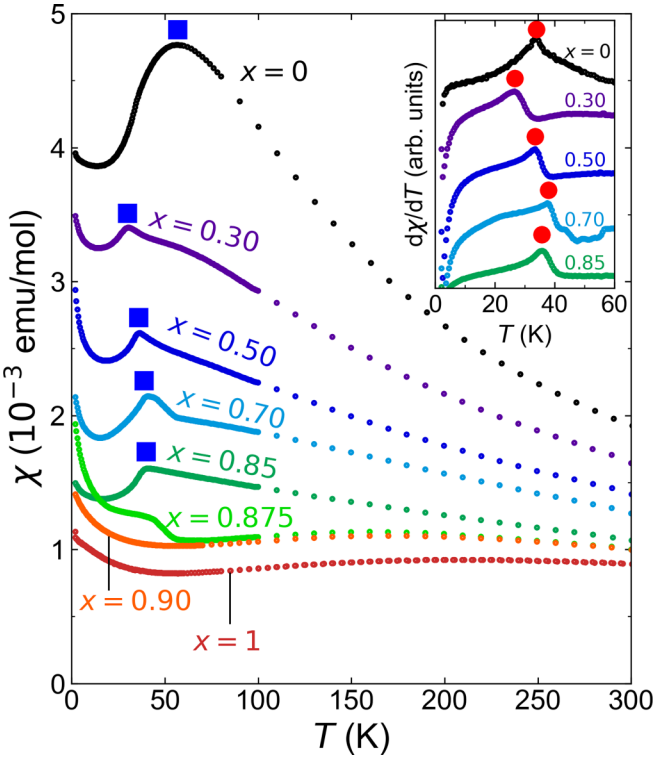

FIG. 3. Temperature T dependence of the magnetic susceptibility χ measured at a magnetic field of $\mu_0 H = 1$ T for $Ru(Br_{1-x}I_x)_3$. Each blue square indicates the temperature T^* where χ is maximum. The inset shows the T dependence of $d\chi/dT$ for $Ru(Br_{1-x}I_x)_3$. Each red circle indicates the temperature $T_{\rm N}$ where $d\chi/dT$ is maximum, below which long-range antiferromagnetic order forms.

and the $j_{\rm eff} = 1/2$ picture is still valid in $RuBr_3$ as evidenced by the Raman spectroscopy [16]. The Weiss temperature $\theta_{\rm W}$ is negative for all compositions, and $|\theta_{\rm W}|$ increases rapidly with increasing x. This means that antiferromagnetic non-Kitaev interactions become dominant compared with the ferromagnetic Kitaev interaction in heavily I-substituted samples. Indeed, the *ab initio* calculations of RuX_3 (X = Cl, Br, I) suggest that stronger d-p hybridization strengthens hopping between next- and third-nearest-neighbor Ru atoms, which leads to stronger long-range exchange interaction with antiferromagnetic character [23]. We note that unrealistically large $|\theta_{\rm W}|$ values in heavily I-substituted samples suggest a breakdown of the localization picture near the insulator-metal transition.

As insulating samples are cooled, two types of anomalies appear in χ: One is a broad peak due to development of an antiferromagnetic correlation at T^*, and the other is a cusp due to the long-range antiferromagnetic order at $T_{\rm N}$ [13]. The latter is clearly evident from $d\chi/dT$ as a sharp peak (inset of Fig. 3) and can be detected via the specific heat at $x = 0$ [13] and $x = 0.85$ (inset of Fig. 4). We plot these characteristic temperatures T^* and $T_{\rm N}$ against x in Fig. 1(b). One can see that T^* and $T_{\rm N}$ have a nonmonotonic x dependence: They decrease at $x = 0$–0.30 but increase at $x = 0.30$–0.85 with increasing x. This hints that the magnetic structure switches from the zigzag order (AFM-I) to another phase (AFM-II) at $x = 0.30$. Moreover, the difference between T^* and $T_{\rm N}$ decreases with increasing x. This indicates that quantum fluctuations related to geometrical frustration are suppressed as the antiferromagnetic non-Kitaev interaction becomes dominant. Particularly, the difference between T^* and $T_{\rm N}$ becomes negligible in the AFM-II phase, indicating that the magnetic order at $x = 0.30$–0.85 is classical. The possible magnetic structures of the AFM-II phase are the stripe, 120°, and checkerboard structures, all of which are discussed in the literature [24].

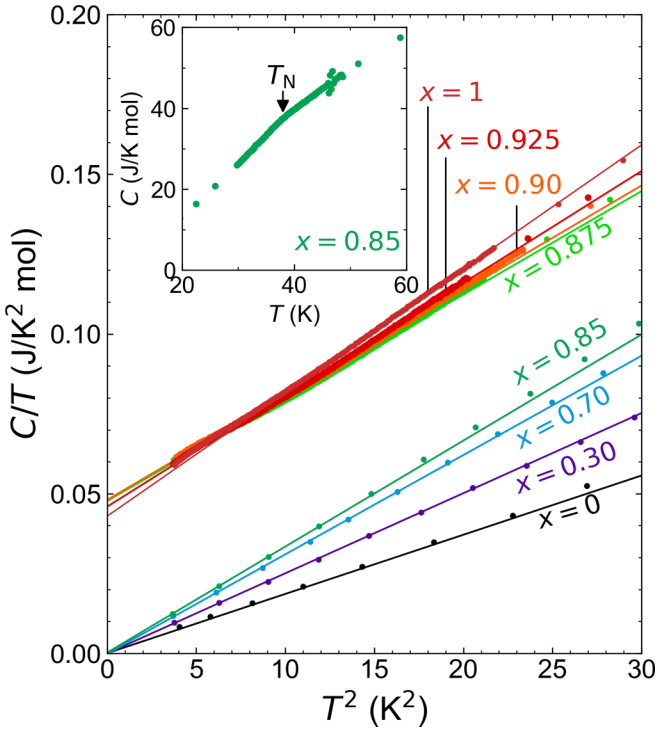

FIG. 4. Specific heat divided by temperature (C/T) plotted against T^2 for $Ru(Br_{1-x}I_x)_3$. The solid lines show the results of fitting with $C/T = \gamma + \beta T^2$. The inset shows the specific heat near the antiferromagnetic transition temperature T_N for $x = 0.85$.

Figure 4 shows the specific heat divided by temperature (C/T) plotted against T^2. The data at $T = 2$–5 K are well fitted with the relationship $C/T = \gamma + \beta T^2$ (fitting results are shown as solid lines), where γ and β are electron and phonon contributions, respectively. We note that magnon contributions are small in this system because the NQR relaxation rate $1/T_1$ for $RuBr_3$ indicates the gapped feature of spin excitations [13]. We calculate the Debye temperature θ_D using the equation $\beta = 12\pi^4 n N_A k_B / 5\theta_D^3$, where $n = 4$ is the number of atoms in the molecular formula. The obtained θ_D and γ values are plotted against x in Fig. 1(d).

We first discuss phonon contributions. One can see that θ_D monotonically decreases with increasing x, which is a consequence of the heavy mass of I atoms compared with that of Br atoms. The Debye temperature follows distinct curves between $0 \leqslant x \leqslant 0.85$ and $0.85 \leqslant x \leqslant 1$. This is related to the phonon frequency change due to the possible structural transition at $x \sim 0.85$. The Debye temperature in solid solution $A_{1-x}B_x$ is known to obey the Neumann-Kopp rule $1/\theta_{AB}^3 = (1-x)/\theta_A^3 + x/\theta_B^3$, where θ_A and θ_B are the Debye temperatures of A and B, respectively. In our system, we need to apply this rule to the data at $0 \leqslant x \leqslant 0.85$ and $0.85 \leqslant x \leqslant 1$ separately, and the results are shown as a solid curve in Fig. 1(d). The application works well for $Ru(Br_{1-x}I_x)_3$.

We next discuss electron contributions. The Sommerfeld coefficient γ is finite at $x = 0.875$–1. Most importantly, γ is enhanced when one approaches the critical region of the insulator-metal transition from $x = 1$ to $x = 0.875$. This behavior can be well understood in the Brinkman-Rice scenario, which claims that the carrier localization is triggered by mass enhancement [25]. Furthermore, the Wilson ratio $R_W = \pi^2 k_B^2 \chi / 3\mu_B^2 \gamma$ is an indicator of electron correlation strength [26]. The calculated values are $R_W = 1.6$ at $x = 0.875$ and $R_W = 1.4$ at $x = 1$ (χ is estimated by subtracting the Curie tail from the data), which also indicate a moderately enhanced quasiparticle mass near the critical region.

We now discuss the microscopic mechanism of the insulator-metal transition in $Ru(Br_{1-x}I_x)_3$. The theoretical analysis based on the single-band Hubbard model with a honeycomb structure predicts that the bandwidth-controlled insulator-metal transition will occur continuously [27], which does not agree with our observation in $Ru(Br_{1-x}I_x)_3$. Here, we discuss the reason why the insulator-metal transition is of the first order in $Ru(Br_{1-x}I_x)_3$. First, we need to explain the multiband features of $Ru(Br_{1-x}I_x)_3$, which are clearly seen in the electrical resistivity data. The model Hamiltonian of $Ru(Br_{1-x}I_x)_3$ cannot be a single-band Hubbard model, which is the reason for the discrepancy with the theoretical prediction. The second possibility is that the structural instability is also a key factor in the insulator-metal transition. The structural change at $x \sim 0.85$ is most likely the formation of interlayer I–I bonds. Such bond formation frequently accompanies the charge transfer from anions to cations. This self-doping effect drives the insulator-metal transition. This type of insulator-metal transition is reported in the layered material $1T$-$Cr(Se_{1-x}S_x)_2$, in which the formation of interlayer Se–Se bonds plays the key role [28]. To verify this, the determination of Ru valence is important and left for a future work.

Even though the insulator-metal transition in $Ru(Br_{1-x}I_x)_3$ has a first-order nature, we could observe the quantum critical phenomenon that γ moderately diverges towards the insulator-metal transition. This behavior is consistent with the theoretical prediction for a single-band Hubbard model with a honeycomb lattice, which predicts that the quasiparticle weight decreases in the quantum critical region following the Gross-Neveu universality class [27]. This possibility could be further verified by observing a divergence in the self-energy via angle-resolved photoemission spectroscopy and confirming the checkerboard magnetic structure in the AFM-II phase via neutron diffraction measurements.

In summary, we successfully synthesized solid solution $Ru(Br_{1-x}I_x)_3$ with honeycomb structure (space group $R\bar{3}$) and investigated its electronic properties. We observed a first-order insulator-metal transition at $x \sim 0.85$, which is likely affected by the formation of interlayer I–I bonds. We also found switching of the magnetic structure from zigzag order at $x = 0$–0.30 to another phase at $x = 0.30$–0.85. Furthermore, the Sommerfeld coefficient γ is moderately enhanced from $x = 1$ to $x = 0.875$, which indicates that the carrier is localized owing to the effective mass enhancement.

Note added. Recently, we noticed a related work [29], which discusses electronic properties from a slightly different point of view.

We would like to thank K. Nawa, T. J. Sato, H. Suzuki, and Y. Yamaji for fruitful discussions and T. Yajima for help with the PXRD measurements. This work was performed using the facilities of the Materials Design and Characterization Laboratory in the Institute for Solid State

Physics, The University of Tokyo (Grants No. 202112-MCBXG-0024 and No. 202205-MCBXG-0072). This work was financially supported by JSPS KAKENHI Grants No. JP19H05823, No. JP19H05822, No. JP22H00102, No. JP22H01175, and No. JP22K18680 and by JST CREST Grant No. JP19198318.

[1] M. Imada, A. Fujimori, and Y. Tokura, Rev. Mod. Phys. **70**, 1039 (1998).
[2] W. Witczak-Krempa, G. Chen, Y. B. Kim, and L. Balents, Annu. Rev. Condens. Matter Phys. **5**, 57 (2014).
[3] K. Ohgushi, H. Gotou, T. Yagi, Y. Kiuchi, F. Sakai, and Y. Ueda, Phys. Rev. B **74**, 241104(R) (2006).
[4] K. Ueda, T. Oh, B.-J. Yang, R. Kaneko, J. Fujioka, N. Nagaosa, and Y. Tokura, Nat. Commun. **8**, 15515 (2017).
[5] A. Kitaev, Ann. Phys. (Amsterdam) **321**, 2 (2006).
[6] G. Jackeli and G. Khaliullin, Phys. Rev. Lett. **102**, 017205 (2009).
[7] Y. Nagai, T. Jinno, J. Yoshitake, J. Nasu, Y. Motome, M. Itoh, and Y. Shimizu, Phys. Rev. B **101**, 020414(R) (2020).
[8] H.-S. Kim, V. Vijay Shankar, A. Catuneanu, and H.-Y. Kee, Phys. Rev. B **91**, 241110(R) (2015).
[9] J. A. Sears, M. Songvilay, K. W. Plumb, J. P. Clancy, Y. Qiu, Y. Zhao, D. Parshall, and Y.-J. Kim, Phys. Rev. B **91**, 144420 (2015).
[10] C. Balz, L. Janssen, P. Lampen-Kelley, A. Banerjee, Y. H. Liu, J.-Q. Yan, D. G. Mandrus, M. Vojta, and S. E. Nagler, Phys. Rev. B **103**, 174417 (2021).
[11] Y. Kasahara, S. Suetsugu, T. Asaba, S. Kasahara, T. Shibauchi, N. Kurita, H. Tanaka, and Y. Matsuda, Phys. Rev. B **106**, L060410 (2022).
[12] S. Suetsugu, Y. Ukai, M. Shimomura, M. Kamimura, T. Asaba, Y. Kasahara, N. Kurita, H. Tanaka, T. Shibauchi, J. Nasu, Y. Motome, and Y. Matsuda, J. Phys. Soc. Jpn. **91**, 124703 (2022).
[13] Y. Imai, K. Nawa, Y. Shimizu, W. Yamada, H. Fujihara, T. Aoyama, R. Takahashi, D. Okuyama, T. Ohashi, M. Hagihala, S. Torii, D. Morikawa, M. Terauchi, T. Kawamata, M. Kato, H. Gotou, M. Itoh, T. J. Sato, and K. Ohgushi, Phys. Rev. B **105**, L041112 (2022).
[14] K. Nawa, Y. Imai, Y. Yamaji, H. Fujihara, W. Yamada, R. Takahashi, T. Hiraoka, M. Hagihala, S. Torii, T. Aoyama, T. Ohashi, Y. Shimizu, H. Gotou, M. Itoh, K. Ohgushi, and T. J. Sato, J. Phys. Soc. Jpn. **90**, 123703 (2021).
[15] D. Ni, X. Gui, K. M. Powderly, and R. J. Cava, Adv. Mater. **34**, 2106831 (2022).
[16] Y. Choi, J.-H. Lee, S. Lee, D. Wulferding, H. Fujihara, F. Sato, Y. Imai, K. Ohgushi, M.-J. Seong, and K.-Y. Choi, Phys. Rev. B **106**, 174430 (2022).
[17] Y. Zhang, L.-F. Lin, A. Moreo, and E. Dagotto, Phys. Rev. B **105**, 085107 (2022).
[18] K. Momma and F. Izumi, J. Appl. Crystallogr. **44**, 1272 (2011).
[19] H.-S. Kim, Appl. Sci. Convergence Technol. **30**, 191 (2021).
[20] We also note the possibility that the tiny anomaly at $T = 40$ K for $x = 0.85$ is related to the band folding due to an antiferromagnetic transition.
[21] We note the possibility that the χ anomaly at $T \sim 50$ K for $x = 0.875$ is related to the development of an antiferromagnetic correlation.
[22] Y. Li, S. M. Winter, D. A. S. Kaib, K. Riedl, and R. Valentí, Phys. Rev. B **103**, L220408 (2021).
[23] D. A. S. Kaib, K. Riedl, A. Razpopov, Y. Li, S. Backes, I. I. Mazin, and R. Valentí, npj Quantum Mater. **7**, 75 (2022).
[24] J. G. Rau, E. K.-H. Lee, and H.-Y. Kee, Phys. Rev. Lett. **112**, 077204 (2014).
[25] W. F. Brinkman and T. M. Rice, Phys. Rev. B **2**, 4302 (1970).
[26] K. Wilson, Rev. Mod. Phys. **47**, 773 (1975).
[27] Y. Otsuka, S. Yunoki, and S. Sorella, Phys. Rev. X **6**, 011029 (2016).
[28] S. Kobayashi, N. Katayama, T. Manjo, H. Ueda, C. Michioka, J. Sugiyama, Y. Sassa, O. K. Forslund, M. Månsson, K. Yoshimura, and H. Sawa, Inorg. Chem. **58**, 14304 (2019).
[29] D. Ni, X. Xu, and R. J. Cava, arXiv:2311.13645.